# Rutile (β-)MnO$_2$ Surfaces and Vacancy Formation for High Electrochemical and Catalytic Performance

David A. Tompsett,* Stephen C. Parker, and M. Saiful Islam*

Department of Chemistry, University of Bath, Bath BA2 7AY, U.K.

ⓢ Supporting Information

ABSTRACT: MnO$_2$ is a technologically important material for energy storage and catalysis. Recent investigations have demonstrated the success of nanostructuring for improving the performance of rutile MnO$_2$ in Li-ion batteries and supercapacitors and as a catalyst. Motivated by this we have investigated the stability and electronic structure of rutile (β-)MnO$_2$ surfaces using density functional theory. A Wulff construction from relaxed surface energies indicates a rod-like equilibrium morphology that is elongated along the c-axis, and is consistent with the large number of nanowire-type structures that are obtainable experimentally. The (110) surface dominates the crystallite surface area. Moreover, higher index surfaces than considered in previous work, for instance the (211) and (311) surfaces, are also expressed to cap the rod-like morphology. Broken coordinations at the surface result in enhanced magnetic moments at Mn sites that may play a role in catalytic activity. The calculated formation energies of oxygen vacancy defects and Mn reduction at key surfaces indicate facile formation at surfaces expressed in the equilibrium morphology. The formation energies are considerably lower than for comparable structures such as rutile TiO$_2$ and are likely to be important to the high catalytic activity of rutile MnO$_2$.
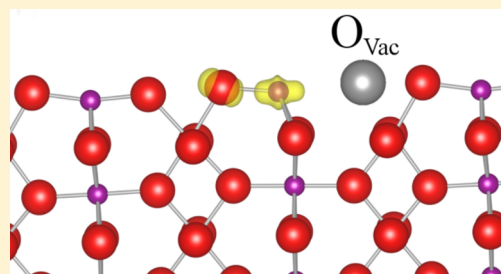
INTRODUCTION

Energy storage for hybrid electric vehicles and renewable energy sources is a pressing technological challenge for which Li-ion batteries and supercapacitors are key candidate systems. The conventional Li-ion intercalation cathode, LiCoO$_2$, faces challenges of toxicity and high cost. Current supercapacitors based on carbon cathodes are limited by their storage capacity. The demand for higher capacity and higher power energy storage has led to a surge in interest in nanostructured electrodes.[1]

Nanostructuring has been shown to improve the energy storage properties of rutile MnO$_2$ for both Li-ion batteries[2,3] and supercapacitors.[4−6] However, the mechanisms for this improvement are not fully understood on the atomic-scale. In addition to its role as an electrode material, nanostructured rutile MnO$_2$ has been shown to give good performance as a catalyst,[7] with much recent interest in its potential role in the Li−O$_2$ battery.[8] Knowledge of the surface features of rutile MnO$_2$ at the atomic and electronic level would provide valuable information regarding its energy storage and catalytic mechanisms. With the clear impetus to better understand the performance of rutile MnO$_2$ in three technologies, Li-ion batteries, supercapacitors and catalysis, in this work we apply first-principles simulations to understand surface phenomena in this promising material.

Rutile MnO$_2$ is the subject of extensive research for its applications in Li-ion batteries, but early work indicated that bulk samples did not allow significant Li-ion intercalation.[2,9,10] However, recent work has reinvigorated interest in the material. Both mesoporous[2,11,12] and needle-like[13,14] nanostructured

rutile MnO$_2$ have demonstrated good intercalation of lithium ions. Both pore size and wall thickness of the mesoporous structures have been shown to affect the rate capability.[15] Furthermore, in recent work we demonstrated that activation barriers for lithium ion migration from the material surface to the bulk of rutile MnO$_2$ may be the rate limiting step for ion diffusion.[16] However, despite the increased importance of nanostructuring, the surfaces of rutile MnO$_2$ have yet to be comprehensively studied for their impact on electrochemical processes. In this work, we use DFT simulations to address the stability of several surfaces up to high indexes, including (331).

Early research into rutile MnO$_2$ for supercapcitors showed limited success for bulk crystallites,[17] which delivered capacities of ∼9 F g^{-1}. However, the formation of nanostructured particles has been demonstrated[18] to dramatically enhance the capacitance to 294 F g^{-1}. Nanostructuring has also been shown to enhance the supercapcitance of other manganese oxides.[19−22] Since the material surface area is critical to electrochemical capacitance, the benefit of nanostructuring is believed to be due to increased material utilization as a result of greater surface area exposure. In this work our simulations of surface morphology indicate a tendency toward elongation along the c-axis that may be advantageous to the formation of nanostructured supercapacitors. Furthermore, the surface structures available for ion adsorption are discussed in detail.

The Li−O$_2$ battery is an alternative chemistry to Li-ion batteries that uses atmospheric oxygen as a reactant and may

offer significant increases in specific energy density.[23,24] In the absence of solvent degradation the aprotic Li−O$_2$ battery is based upon the oxygen reduction reaction (ORR):

$$2Li^+ + O_{2(g)} + 2e^- \rightarrow Li_2O_2, \quad U^o = 2.96\,V \quad (1)$$
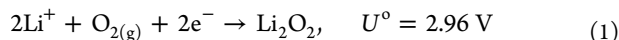
This positive electrode reaction requires the supply of both oxygen and electrons in order that the Li-ions are oxidized. However, experimental work has indicated the presence of overpotentials, 1−1.5 V on charging, and rate limitations.[25,26] Several investigators have suggested the use of transition metal oxides as catalysts to address these issues.[27,28] Rutile MnO$_2$, particularly in nanowire form, has been demonstrated to reduce overpotentials and improve the cycling stability of the Li-oxygen system.[8,29] Recent studies, however, have emphasized the presence of electrolyte decomposition in these earlier works, making the efficacy of catalysts less clear.[30−33] Nevertheless, with more recent demonstrations of the Li−O$_2$ system being cycled with good electrolyte stability[34,35] it is likely that the role of catalysts will become a focus of future studies.

Manganese oxides have also been demonstrated to function as effective catalysts for several other processes: the oxygen reduction reaction in alkaline fuel cells,[36] the oxidation of Cr[III] to Cr[VI],[37,38] the oxidation of toxic As[III] to As[V],[39,40] and water electrolysis.[41] Furthermore, manganese oxides are commonly used as supports in combined catalytic complexes for the oxidation of CO[42,43] and reduction of NOx.[44] Surface terminations and the thermodynamics of oxygen vacancy formation will play important roles in the catalytic activity of rutile MnO$_2$, and we investigate each of these by first-principles simulations in this work. Indeed recent work has shown that the presence of oxygen vacancies at rutile MnO$_2$ surfaces enhances its catalytic activity for the ORR,[45] which makes this investigation of surface properties timely.

Despite the importance of rutile MnO$_2$, particularly in nanostructured form, to these applications, their surface structures and properties are not well understood. An early study of manganese oxide surfaces, including rutile MnO$_2$, applied X-ray photoelectron spectroscopy (XPS).[46] It found evidence for surface reduction of rutile above 400 °C, but did not characterize the surface structure. More recently, electron energy loss spectroscopy (EELS) has been applied to the naturally occurring mineral form of rutile MnO$_2$, pyrolusite. The average valence of the surface was found to be +4.0, in agreement with the formal valence.

Because of growing interest, the surfaces of manganese oxides have recently been the subject of computational studies.[47−54] Maphanga et al.[48] applied interatomic forcefield methods to characterize low index surfaces of rutile MnO$_2$. Sayle et al.[55,56] have also investigated the microstructure and nanoparticle formation of rutile MnO$_2$ using large-scale molecular dynamics methods. Oxford and Chaka[49] applied the generalized gradient approximation (GGA) in density functional theory (DFT) to consider the low index surfaces (110), (100), and (101) of rutile MnO$_2$. They calculated the surface energies of stoichiometric as well as heavily oxidized and reduced surfaces. Their results indicated significant reduction of the surfaces under ultrahigh vacuum conditions (UHV). Oxford and Chaka have also treated the effects of hydration at these surfaces.[50] Since the GGA has been demonstrated to give a poor treatment of the electronic structure of rutile MnO$_2$,[47,57] in this study we incorporate an improved treatment of the on-site Coulomb interactions by applying DFT+U. Furthermore, we treat the surfaces up to higher Miller indexes. A recent study by Cockayne and Li applied DFT+U to study the phase stability of rutile MnO$_2$ in the presence of K$^+$ dopants.[58]

In this work we perform a detailed DFT investigation of rutile MnO$_2$ surfaces. The key questions relate to what surface characteristics are important to, first, electrochemical performance and, second, catalytic activity. The results are organized as follows. First, we outline our computational methods. Then we present results on the structures and energies of stoichiometric surfaces, as well as the equilibrium crystal morphology. Lastly, the calculated energetics of dilute oxygen vacancy formation at surfaces are discussed with reference to catalytic activity.

■ COMPUTATIONAL METHODS

The *ab initio* determination of surface energies and morphologies, particulary in complex and lower symmetry structures, is computationally demanding. Yet the high accuracy of these methods makes their use desirable. Typically, *ab initio* DFT studies are restricted to considering a limited number of surfaces, while the interatomic potentials methods are able to treat more surfaces for the same amount of computer time. In this work we take advantage of the computational efficiency of interatomic potentials to suggest higher index surfaces that are of low energy. These low energy candidates are then treated by DFT which more fully describes the electronic effects in the system.

This study employs well-established interatomic potentials methods, which are reviewed in detail elsewhere.[59−61] The model due to Parker and co-workers,[48,62] that has been utilized successfully in several studies[56,63] of rutile β-MnO$_2$ is employed. The interactions between ions are represented in terms of a long-range Coulmbic term with the addition of an analytic term representing short-range interactions such as chemical bonding. In the model employed these short-range effects are modeled by a Buckingham potential and the full details of the model are presented in the Supporting Information. The model reproduces the lattice parameters of rutile MnO$_2$ within 2% of experiment. In this work we use this accurate interatomic potential model to calculate the surface energies using METADISE[64] up to high indexes.

Candidate low energy surfaces obtained from interatomic potentials were then treated by DFT as implemented in the VASP code[65] with PAW potentials. The electronic structure was calculated using the GGA of Perdew, Burke and Ernzerhof[66] with Hubbard U corrections (PBE+U). The PBE+U exchange-correlation functional has been demonstrated to give a good description of defect properties in other oxides including CeO$_2$[67] and TiO$_2$.[68] To obtain the equilibrium lattice parameters by relaxation of the bulk cell a cutoff for the planewave basis set of 520 eV was used to avoid Pulay stress. All subsequent calculations were performed on the basis of the obtained equilibrium lattice constants without cell relaxation using a cutoff of 400 eV. This included the recalculation of the energy for the bulk unit cell so that all comparative energies were obtained at a constant cutoff of 400 eV. A minimum of 4 × 4 × 4 k-points was used in the Brillouin zone of the conventional cell and scaled appropriately for supercells.

The value of the U parameter for our PBE+U calculations was determined *ab initio* using Wien2k.[69,70] Previous work conducted by some of the present authors[16,47] demonstrated a good description of lithium intercalation, band gaps, and magnetic interactions when PBE+U is applied in the fully localized limit,[71] which we use in this work as well. We employ $(U − J) = 5.1$ eV, for the spherical part of the interaction, and $J = 1.0$ eV. Further details are described in the Supporting Information.

Pristine rutile MnO$_2$ occurs in the tetragonal space group *P4/mnm* (No. 136)[72,73] as shown in Figure 1. The dominant structural building block is the MnO$_6$ octahedra that are edge-sharing along the c-axis and corner sharing in the plane. The PBE+U predicted lattice parameters
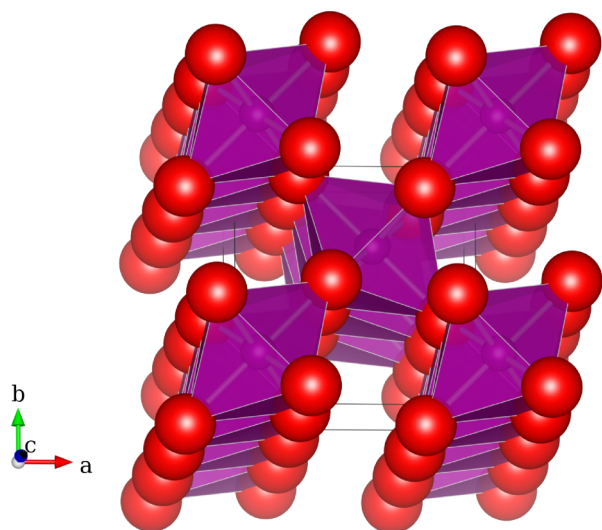
Figure 1. Crystal structure of β-MnO$_2$. Large (red) spheres are oxygen and small (purple) manganese lie inside the indicated approximate MnO$_6$ octahedra. Note the tunnel structure along the c-axis.

shown in Table 1 for β-MnO$_2$ are within 2.5% of those obtained experimentally.

Table 1. Predicted PBE+U and Experimental[72] Lattice Parameters of Rutile MnO$_2$

β-MnO$_2$	a Å	b Å	c Å
PBE+U	4.442	4.442	2.933
experiment	4.398	4.398	2.873

The equilibrium bulk geometry was used to construct surfaces with slab geometries, symmetric about their inversion center, for the calculation of *ab initio* surface energies using VASP. For each surface the slab thickness, minimum of 15 Å, was increased until convergence of the surface energy is obtained. A vacuum thickness greater than 20 Å was used throughout to separate the slabs from their periodic image. Full geometrical relaxation of the ionic positions until the forces fell below 0.02 eV Å^{-2} was performed to incorporate surface relaxation effects. The surface energy was calculated by taking the difference between the energy of the constructued slab and the same number of rutile MnO$_2$ formula units in the bulk:

$$\gamma = \frac{E_s - nE_b}{2A} \qquad (2)$$

Here, E_s is the energy of a slab containing n formula units and E_b is the total energy per formula unit of bulk rutile MnO$_2$. A is the area of the slab surface and the factor of 2 reflects the fact that there are two surfaces for each slab.

To obtain the defect energies with respect to the stoichiometric surface, a single k-point PBE calculation of an isolated spin triplet oxygen molecule in a 15 Å side cubic cell was performed using the same energy cutoff and convergence criterion as for the slab calculations. From this we obtain a reference energy of −9.85 eV for the oxygen molecule. However, the PBE+U functional is known to give rise to errors in formation energies of oxide materials due to both an inadequate description of the oxygen molecule (including overbinding) and of the solid oxides. Consequently, to obtain an estimate of the error as relevant to the process of oxygen vacancy formation with accompanying Mn reduction at rutile MnO$_2$ surfaces we have calculated the enthalpy of the following reaction:

$$MnO_2 \rightarrow \frac{1}{2}Mn_2O_3 + \frac{1}{4}O_2 \qquad (3)$$

This reaction incorporates the removal of oxygen and the reduction of Mn. Comparison of the reaction enthalpy from our PBE+U calculation with the experimental enthalpy (40.5 kJ/mol) of Fritsch et al.[74] indicates a correction of 1.15 eV per oxygen. The correction is applied to all oxygen vacancy formation energies quoted in this work.

■ RESULTS AND DISCUSSION

Surface Energies. Surfaces of rutile MnO$_2$ are important to its electrochemical properties, particularly due to the presence of interfaces in batteries and supercapacitors. Furthermore, surface phenomena are likely to be the basis of the catalytic activity the material shows in a variety of applications. Our methods are able to give insight into important characteristics such as surface terminations and electronic structure at the atomic-scale. In this section we consider stoichiometric surfaces, returning to consider the energetics of oxygen defects in subsequent sections.

For an ionic or partially ionic crystal, it is known that a charged surface with a perpendicular dipole moment will induce a polarizing electric field throughout the crystal, which results in a divergent total energy. Therefore, all such surfaces studied in this work are reconstructed to give a vanishing dipole in the direction of the surface normal.

With only this restriction, we have applied our interatomic potential model to calculate the relaxed surface energies of all surfaces with Miller indices up to order 3. This set includes surfaces (101), (211), (321), and (103) and all other permutations of indexes 0, 1, 2, and 3. This extends the work of Maphanga et al.[48] who calculated the equilibrium surface energies for seven low index surfaces. In contrast, our work screens the surface energy of 29 surfaces.

It is important to note that for a given index several possible surface terminations may be possible since the surface may be cleaved from the crystal at several planes. For instance, we show the two possible cleaving planes for the (101) surface in Figure 2. The illustrated "O-Terminated" surface maintains better 5-
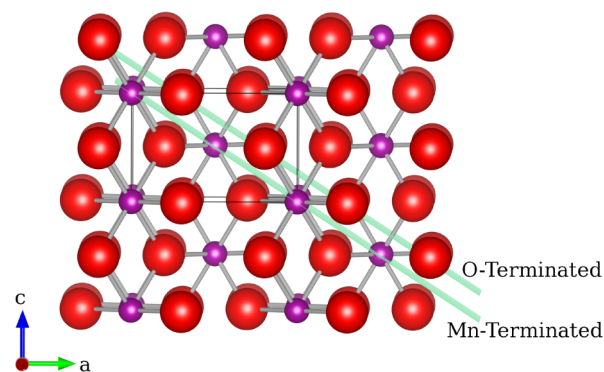

Figure 2. Illustration of the two possible surface terminations, "O-Terminated" and "Mn-Terminated", of the (101) surface that possess a vanishing dipole perpendicular to the surface normal. Large (red) spheres are oxygen and small (purple) manganese.

fold coordination of the Mn near surface ions, while the "Mn-Terminated" surface results in 3-fold coordinate Mn. The impact upon the resulting surface energies is substantial: our interatomic potentials model resulting in a surface energy of 2.15 J m^{-2} for the "O-Terminated" case while the "Mn-Terminated" surface possesses a surface energy of 3.92 J m^{-2}. The multiplicity of terminations emphasizes the large number of calculations that are required to robustly study solid surfaces.

Our approach of determining the energies of numerous surfaces with interatomic potentials, followed by the inclusion of electronic structure effects with PBE+U, is well adapted to this problem.

In Table S1 of the Supporting Information we list all of the obtained converged surface energies calculated with our interatomic potential model. We find good agreement with the results of Maphanga et al.[62] for low index surfaces. The lowest energy is obtained for the (110) surface. Furthermore, it is clear that some higher index surfaces also possess low energies, for instance the oxygen terminated (311) surface is less than 0.5 J m^{-2} higher in energy. On the basis of these surface energies we take all surfaces that are expressed in the resulting Wulff constructed morphology, or are near to expression, forward to be treated by *ab initio* PBE+U.

In Table 2 we show the obtained PBE+U surface energies of all low index surfaces as well as the surfaces brought forward

Table 2. Predicted PBE+U Surface Energies for β-MnO$_2$

miller index	surface energy γ (J m^{-2})
(100)	0.94
(001)	1.80
(110)	0.62
(111)	1.42
(101)	1.59
(201)	1.41
(211)	1.12
(221)	2.54
(311)	1.08
(321)	1.01
(331)	3.59

from the interatomic potentials. It is clear that the (110) surface possesses the lowest energy at 0.62 J m^{-2} consistent with the results from interatomic potentials. It is also clear from the table that higher index facets do not necessarily result in higher surface energies. For instance the (211) and (311) surfaces have an energy of 1.12 J m^{-2} and 1.08 J m^{-2}, respectively, but were neglected in previous DFT studies. Therefore, important higher index surfaces suggested to be low in energy by our interatomic potentials retain low energies when treated with PBE+U. We will return to discuss the surface terminations and their relevance to technological applications in detail.

We note that the order of stability of the three low index surfaces studied by Oxford and Chaka[49] is the same as that obtained in our work. In that work they calculated $\gamma(110) = 0.83$ J m^{-2}, $\gamma(100) = 1.03$ J m^{-2}, and $\gamma(101) = 1.28$ J m^{-2}. The small differences in absolute surface energy compared to our results are likely a result of their use of the PBE-GGA functional, which does not treat the on-site correlations of the Mn *d*-states as fully as our PBE+U approach.[47,57] Futhermore, Oxford and Chaka treated only three low index surfaces, while the present work highlights the potential importance of other low index surfaces such as the (001) and high index surfaces such as the (211) and (311) surfaces. We note that Oxford and Chaka also considered off-stoichiometry at these surfaces, but found the stoichiometric surfaces to be the most stable at experimentally accessible conditions. In this work we treat surface reductions, but with an emphasis on *dilute* oxygen vacancy formation due to first, its relevance to catalysis and second, its energetic favorability at experimental conditions.

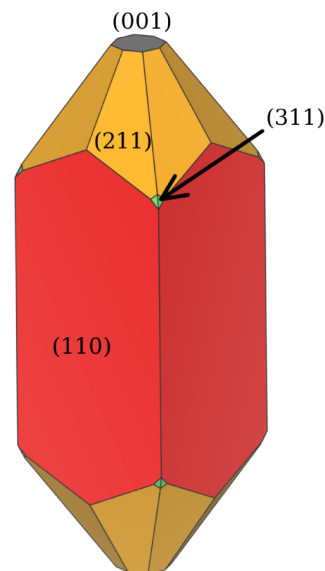**Crystal Morphology.** The resulting equilibrium morphology from the calculated energies in Table 2 is shown in Figure 3

Figure 3. The predicted equilibrium crystal morphology for rutile MnO$_2$ based upon the surface energies in Table 2

and forms an elongated rod structure which is approximately three times as long as it is wide. The shape may be described as being like a short pencil that has been sharpened at both ends. The tendency toward an elongated rod-like structure may be important to the nanorod and nanotube-type[75−78] morphologies of rutile MnO$_2$ that have shown promising electrochemical performance as battery cathodes, oxygen reduction catalysts,[79,80] and supercapacitors.[81] By considering higher Miller indexes than treated in previous computational studies, we bring to light the importance of new surfaces of importance to the properties of this system. Consistent with previous work[48] the (110) surface possesses a low energy and represents 64% of the surface area of this crystal morphology.

Our predicted elongated morphology is consistent with the experimentally synthesized MnO$_2$ nanorods from several studies.[8,82−85] Indeed, the dominance of the (110) surface has been experimentally demonstrated by high resolution transmission electron micrography (HRTEM) by the isolation of fringe spacings commensurate with this surface.[85] The higher index (211) surface plays an important role in terminating our predicted morphology along the *c*-axis. The (311) surface is expressed, but represents less than 2% of the exposed surface area. Furthermore, the (001) surface caps the ends of the morphology. The primary difference between our predicted morphology and that of previous interatomic potentials work[62] is the absence of the (101) surface from our Wulff construction. This arises because the higher index (211) and (311) surfaces were not treated in that work. Furthermore, although the conventional wisdom is that high index surfaces generally result in poorer surface coordination, in rutile MnO$_2$ these high index surfaces possess good surface coordination. We will return to discuss these characteristics in detail for key surfaces.

Surface Structures and Magnetic Moments. The importance of surface structural relaxation in these systems has been emphasized before,[62] and here we also find it is critical to lowering the energies of important surfaces. For instance the (110) has an unrelaxed surface energy of 0.94 J m^{-2} that is

reduced to 0.62 J m^{-2} with structural relaxation effects, a reduction of more than 30%. Many of the low energy surfaces are primarily oxygen terminated.

The (110) surface structure is shown before and after relaxation in Figure 4. The Mn site labeled Mn(2) has a
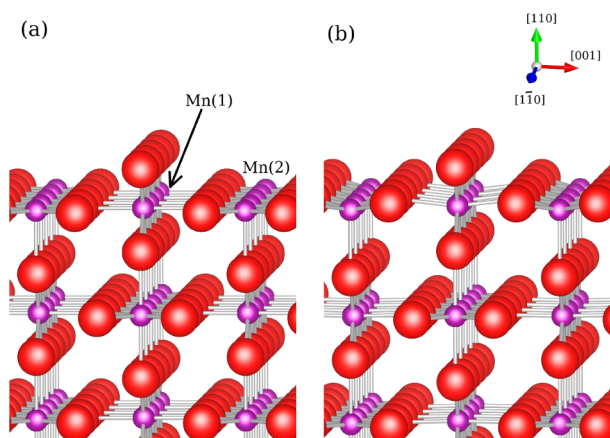

Figure 4. Structure of the (110) surface of β-MnO$_2$: (a) before relaxation and (b) after relaxation.

reduced 5-fold oxygen coordination after the surface is cleaved. The dominant relaxation at this surface is the movement of oxygen ions that are attached to this Mn site away from the surface to better coordinate Mn(2). This outward buckling of neighboring oxygen species is apparent from the relaxed structure of Figure 4b. Undercoordinated oxygen anions are likely to be adsorption sites for hydrogen ions when rutile MnO$_2$ is used as a supercapacitor electrode.

In Table 3 we summarize the coordination numbers and magnetic moments for the surface Mn ions of the low energy

Table 3. Predicted Mn Coordinations and Magnetic Moments for Low Energy Surfaces of β-MnO$_2$. Surface Mn-Ions Are Labeled as in Figures 4−7.

surface	site	n_{coord}	moment (μ_B)
(110)	Mn(1)	6	3.14
	Mn(2)	5	3.75
(001)	Mn(1)	4	3.72
(211)	Mn(1)	5	3.36
	Mn(2)	4	3.86
(311)	Mn(1)	4	3.79
	Mn(2)	5	3.36
	Mn(3)	5	3.74
bulk	Mn(1)	6	3.09

surfaces. From the final column it is clear that the 5-fold coordinate Mn(2) ion at (110) possesses an enhanced magnetic moment of 3.75 μ_B compared to 3.09 μ_B for bulk sites. Such enhanced magnetic moments have recently also been observed[86] at the surface of nanosized stoichiometric LiCoO$_2$. We find that the surface energies of rutile MnO$_2$ may be strongly affected by whether the surface is relaxed with the correct spin enhancement. This demonstrates the utility of treating the electronic structure of magnetic oxide surfaces, which we have done here with *ab initio* PBE+U.

For the (110) surface the Mn(2) ion lies in a square-pyramidal coordination, which in general alters the order of stability of Mn-d orbitals due to the change in crystal field. In

the perfect octahedral coordination of the bulk crystal the three t$_{2g}$ orbitals (xy, xz, and yz) lie energetically lower than the two e$_g$ orbitals (z^2 and $x^2 - y^2$). However, in a square-pyramidal coordination the t$_{2g}$ orbitals are split into two lower (xz and yz) and an upper (xy) orbital. Furthermore, the higher e$_g$ orbitals are also split so that the z^2 orbital is reduced in energy due to the absence of an apical oxygen, and therefore lies below the uppermost $x^2 - y^2$ orbital. In previous work[47] we demonstrated that the z^2 orbital possesses a very low spin moment of 0.09 μ_B in bulk rutile MnO$_2$. However, the removal of an apical oxygen reduces the role of this orbital in bonding resulting in an enhanced moment due to the action of the Hund's coupling which is now the dominant energy scale over bonding. Analysis of the Bader charge also indicates that the undercoordinated Mn(2) possesses an enhanced charge of 5.02 compared to 4.83 electrons for bulk Mn ions. Simultaneously the Bader charge on the outermost surface oxygen decreases to ~6.7 from 7.1 electrons in the bulk. This represents a charge transfer from surface oxygen to surface Mn and is suggestive of a more covalent character or weak metal−metal interactions. The latter has already been implicated in affecting bulk magnetic properties.[47]

The (001) surface is terminated by a charge neutral layer consisting of both Mn- and O-ions as shown in Figure 5. The
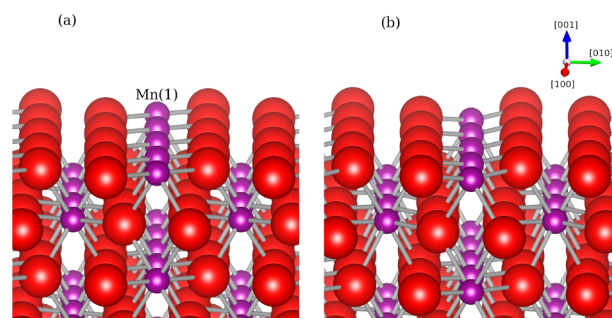

Figure 5. Structure of the (001) surface of β-MnO$_2$: (a) before relaxation and (b) after relaxation.

primary relaxation is the buckling of surface oxygens outward from the surface to make the negative charge sphere around the 4-fold coordinate Mn(1)-ion more spherical. The O−Mn(1)−O bond angle, which is a perfect 180° before relaxation, becomes 168°. Furthermore, the undercoordination of the Mn(1) ion results in an enhanced magnetic moment on Mn(1) of 3.72 μ_B. Inspection of the Mn(1)−O bond lengths for this (001) surface indicates that the low coordination number of this Mn-ion results in reduced bond lengths. It is noted that the under coordination of the Mn-ion is likely to raise the energy for oxygen defect formation at this surface, since oxygen removal will result in unfavorable 3-fold coordinate Mn sites.

In Figure 6 we compare the (211) surface before and after structural relaxation. The movement of the outermost oxygen ions that bridge the manganese rows dominates. These oxygen ions move out from the surface and to a more medial position with respect to the manganese rows formed by Mn(1) and Mn(2). This results in a shortened bond length from 4-fold coordinated Mn(2) to this oxygen of just 1.822 Å and from 5-fold Mn(1) of 1.825 Å. It is important to stress the low surface energy, 1.12 J m^{-2}, of this (211) surface despite its high Miller index. As noted, previous studies have not treated such high Miller indexes, but it is clear that the rutile structure permits good coordination of the surface manganese ions for the (211)
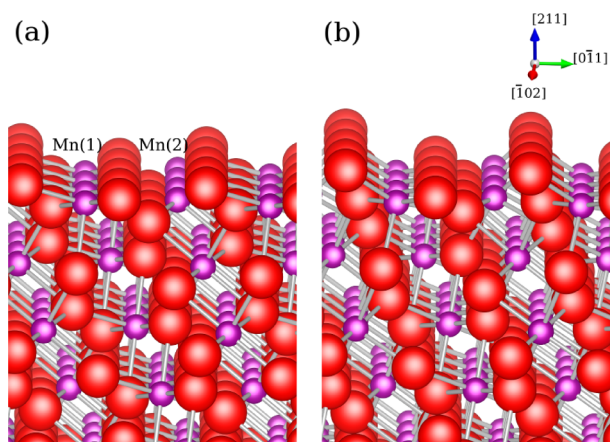
Figure 6. Structure of the (211) surface of β-MnO$_2$: (a) before relaxation and (b) after relaxation.

surface. The two surface manganese ions are 4-fold and 5-fold coordinate, which is the same average coordination or better than any low index surface that has a component perpendicular to the c-axis, that is, surfaces that are able to cap the morphology in Figure 3. The (001) surface has an average coordination number of 4 for surface manganese, while the (101) and (111) have the same average coordination as the (211) surface of 4.5.

The potential for high Miller index surfaces to possess good surface Mn coordination and low surface energy is emphasized by the expression of the (311) surface in the morphology. The (311) surface gives an average surface Mn coordination of 4 2/3. This surface also undergoes substantial relaxations dominated by significant outward movements of oxygen ions. These movements help to fill the empty coordination space left by cleaving the surface as shown in Figure 7. This surface has a corrugated appearance which may offer good coordination at adsorption sites for catalytic processes.
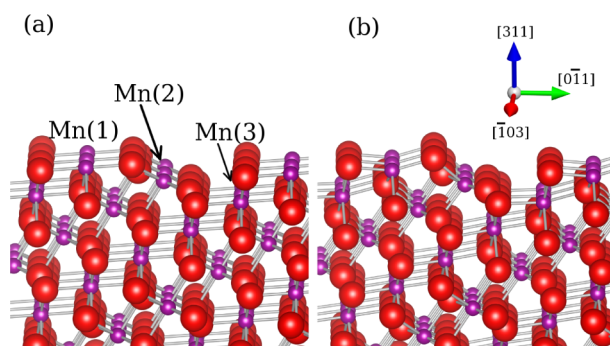

Figure 7. Structure of the (311) surface of β-MnO$_2$: (a) before relaxation and (b) after relaxation.

Finally, we note the potential for surface reconstructions to improve the coordination of the Mn surface sites and alter the surface energies. For instance, among the surfaces studied we identified that the (111) surface energy could be reduced from 2.06 J m^{-2} to 1.42 J m^{-2} by transferring a surface oxygen from a 6-fold Mn site to a 3-fold site. The details of this reconstruction are presented in detail in the Supporting Information. However, even after reconstruction the (111) surface is not expressed in the equilibrium morphology. Reconstructions at other surfaces

are of potential importance, but due to the large available configuration space will be the subject of future work.

Oxygen Vacancy Formation and Catalytic Activity. The process of oxygen defect formation at MnO$_2$ surfaces may play a key role in its catalytic activity. For instance, the Mars-van Krevelen mechanism[87] requires a redox process in which oxygen is consumed from the surface and then replenished from the gas phase. Indeed, a recent combined experimental and DFT work[45] demonstrated that oxygen vacancy formation at rutile MnO$_2$ surfaces enhances catalytic activity for the ORR, particularly at the (110) surface. However, the thermodynamics for the formation of the required oxygen vacancies in the first place was not addressed, which we address here.

Other simulation studies have considered the reaction mechanism of Li−O$_2$ involving adsorption/desorption processes at lithium oxide,[88] Au/Pt[89] and carbon[90] surfaces. Oxford et al. have studied the thermodynamics of low Miller index ((110), (100), and (101)) surfaces with high concentrations of oxygen vacancies, but none of the reduced surfaces were found to be energetically favorable at experimentally relevant conditions. Rather it is dilute, low concentration, oxygen vacancies that are likely to be active in catalysis, and it is these that are treated by our work. Vacancy formation energies have been calculated according to the following reduction process:

$$\text{O}_\text{O}^\times + 2\text{Mn}_\text{Mn}^\times \rightarrow \text{V}_\text{O}^{\bullet\bullet} + 2\text{Mn}_\text{Mn}' + \frac{1}{2}\text{O}_{2(\text{g})} \qquad (4)$$

where Kroger−Vink notation has been used. Here, the lattice site that a species occupies is indicated by the subscript, and the superscript shows the electric charge of the species relative to that of the charge of that site in a stoichiometric crystal: × indicates no change to the charge, a single prime (′) represents a negative charge, and a bullet (•) represents a positive charge.

The defect energies for removal of all symmetry inequivalent surface oxygens have been calculated and the lowest defect energy obtained for each surface is shown in Table 4. All defect

Table 4. Formation Energies Based on Equation 4 for the Most Favorable Dilute Oxygen Vacancy at Surfaces of β-MnO$_2$. Surfaces of Low Index and Those That Are Expressed in the Morphology of Figure 3 Are Presented

Miller Index	$\Delta E_\text{F}(\text{O}-\text{vac})$ (eV)
(100)	1.13
(101)	1.26
(111)	1.41
(001)	1.43
(110)	0.98
(211)	1.09
(311)	0.96
Bulk	2.26

energies were converged with respect to slab thickness and surface cell expansion ($u \times v$) to their values in the dilute limit (to within 0.02 eV). In Supporting Information Figures S1 and S2 we show plots of the convergence of the defect energy with respect to these parameters. Consequently, we may be confident in the relative order of stability of the defect formation energies for the various surfaces shown in Table 4. The key result is that the lowest defect formation energies occur for three surfaces (110), (211), and (311) that are expressed in the calculated crystal morphology. Furthermore,

the defect formation energies at these surfaces are all low and favorable, particularly compared to those obtained for similar materials such as rutile TiO_2, where oxygen vacancy formation energies at surfaces are calculated to be 2–5 eV.[68,91] This may aid in explaining the favorable performance of MnO_2 in important catalytic applications. Furthermore, the lowest defect formation energy occurs for the (311) followed by the (110) surface which agrees well with the experimental assignment of Poinsignon et al.[92] from slow step linear voltammetry reduction.

The calculated formation energy for an oxygen vacancy in the bulk is 2.26 eV. Therefore, oxygen vacancy formation in the bulk is less favorable than at any of the surfaces studied here. The more facile vacancy formation at surfaces of rutile MnO_2 may be a key contributor to its enhanced catalytic performance in nanostructured form. We also note the potential for cation interstitial formation in the subsurface to compete with surface oxygen vacancy formation. Our focus in this study has been on oxygen vacancy formation with relevance to catalysis, but the formation of Mn interstitials warrants further investigation.

The (001) surface is expressed in the equilibrium morphology, but possesses a significantly higher defect formation energy than the other expressed surfaces at +1.43 eV. This may be readily understood by the fact that the oxygen vacancy formation leaves the presence of 3-fold coordinate manganese sites.

Oxygen vacancy formation results in sharp spin-polarized gap states (associated with $V_O^{\bullet\bullet}$ or Mn'_{Mn}) in the band gap of the density of states. In Figure 8 we plot the charge density associated with the defect induced states for surfaces expressed in the calculated morphology. For the (110) surface, charge density associated with this defect peak resides primarily on the two nearest neighbor Mn-ions as shown in Figure 8a. Furthermore, the orbital lobes are angled away from the surface to protrude into a space where they may participate in surface reactivity. For the (001) surface in Figure 8b the charge density is associated with the Mn-ion nearest the vacancy and its adjacent oxygen atom.

At the stoichiometric (211) surface we obtain a sharp occupied defect state below the Fermi level and the charge associated with this occupied state is localized on one surface and a subsurface manganese site with significant hybridization to a deeper oxygen site as shown in Figure 8c.

For the (311) surface we obtain a qualitatively different behavior where the insulating stoichiometric surface becomes metallic upon vacancy formation, resulting in the defect charge occupying itinerant states that straddle the Fermi level. Oxygen vacancy defects have been implicated in creating metallic conductivity in experimental studies of bulk[93] and nanostructured[94] rutile MnO_2, and were recently shown to arise at surfaces of lithium peroxide by DFT.[95] The metallic states are distributed over both oxygen and manganese sites. Clearly, the production of metallic states upon oxygen vacancy formation will depend upon the defect concentration, but the observed behavior is consistent with the intermediate ionic-covalent character of rutile MnO_2. The detailed electronic structure at these surfaces will be explored further in a subsequent publication.

■ CONCLUSIONS

The present study has used density functional theory to deepen our understanding of the surface properties of rutile MnO_2, an
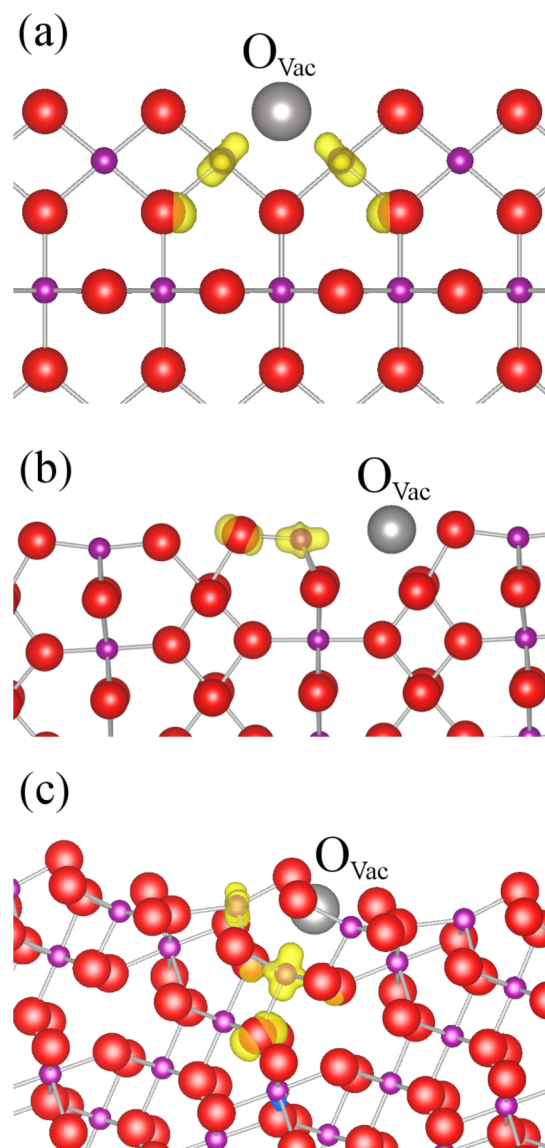

Figure 8. Charge density isosurfaces associated with defect states for expressed surfaces: (a) (110), (b) (001), and (c) (211). The large gray sphere indicates the position of the oxygen vacancy, O_{Vac}.

important material for energy storage and catalysis applications. The primary findings include the following:

(1) The equilibrium crystal morphology has a rod-like form, with the (110) surface accounting for 64% of the available surface area. By considering surfaces up to higher Miller index than in previous studies we demonstrate that the (211) and (311) surfaces are candidate low energy facets. The tendency toward a rod-like structure may be important to the formation of nanomorphologies that have shown promising electrochemical performance as battery cathodes, oxygen reduction catalysts, and supercapacitors.

(2) The coordination of the manganese sites at the surface plays an important role in the system with respect to both crystalline order and electronic structure. For instance the (110) surface, that possesses the lowest calculated surface energy, has an average manganese coordination of 5 1/2, which is close to the bulk value of 6. Furthermore, undercoodinated manganese surface sites are shown to possess enhanced

magnetic moments, which may play a role in the complex surface electronic structure and catalytic activity of rutile MnO_2.

(3) Formation energies for the defect process involving oxygen vacancy creation and manganese reduction at surfaces are calculated to be lowest for three surfaces expressed in the equilibrium morphology, following the trend $\Delta E_F(311) < \Delta E_F(110) < \Delta E_F(211) < \Delta E_F(001)$. The defect energies for all of these surfaces are in the low range of 0.95 to 1.5 eV. These energies are significantly lower than for similar materials such as rutile TiO_2 where the defect formation energies are calculated to lie in the range 2−5 eV. It is likely that the low energies to form surface oxygen vacancies are important to the good catalytic activity of rutile MnO_2, for instance in application to $Li-O_2$ batteries.

ASSOCIATED CONTENT

Ⓢ Supporting Information

Tables describing the full definition of our interatomic potential model and the calculated surface energies from this model; figure of the resulting equilibrium Wulff morphology from interatomic potentials; discussion of technical details of our PBE+U methodology; detailed discussion of the reconstruction at the (111) surface with an associated figure of the reconstruction; discussion and two figures detailing the convergence of our defect formation energies to the dilute limit. This material is available free of charge via the Internet at http://pubs.acs.org.

AUTHOR INFORMATION

Corresponding Author

dt331@bath.ac.uk; m.s.islam@bath.ac.uk

Notes

The authors declare no competing financial interest.

ACKNOWLEDGMENTS

REFERENCES

(1) Arico, A. S.; Bruce, P. G.; Scrosati, B.; Tarascon, J. M.; Van Schalkwijk, W. *Nat. Mater.* **2005**, *4*, 366.

(2) Jiao, F.; Bruce, P. G. *Adv. Mater.* **2007**, *19*, 657.

(3) Ren, Y. Ph.D. Thesis, University of St. Andrews, U.K., 2010.

(4) Lang, X.; Hirata, A.; Fujita, T.; Chen, M. *Nat. Nanotechnol.* **2011**, *6*, 232.

(5) Subramanian, V.; Zhu, H.; Vajtai, R.; Ajayan, P. M.; Wei, B. *J. Phys. Chem. B* **2005**, *109*, 20207.

(6) Zhang, H.; Cao, G.; Wang, Z.; Yang, Y.; Shi, Z.; Gu, Z. *Nano Lett.* **2008**, *8*, 2664.

(7) Andreozzi, R.; Insola, A.; Caprio, V.; Marotta, R.; Tufano, V. *Appl. Catal., A* **1996**, *138*, 75.

(8) Debart, A.; Paterson, A. J.; Bao, J.; Bruce, P. G. *Angew. Chem., Int. Ed.* **2008**, *47*, 4521.

(9) Thackeray, M. M.; Johnson, C. S.; Vaughey, J. T.; Li, N.; Hackney, S. A. *J. Mater. Chem.* **2005**, *15*, 2257.

(10) Kijima, N.; Sakata, Y.; Takahashi, Y.; Akimoto, J.; Kumagai, T.; Igarashi, K.; Shimizu, T. *Solid State Ionics* **2009**, *180*, 616.

(11) Luo, J.-Y.; Zhang, J.-J.; Xia, Y.-Y. *Chem. Mater.* **2006**, *18*, 5618.

(12) Mathew, V.; Lim, J.; Kang, J.; Gim, J.; Rai, A. K.; Kim, J. *Electrochem. Commun.* **2011**, *13*, 730.

(13) Cheng, F.; Zhao, J.; Song, W.; Li, C.; Ma, H.; Chen, J.; Shen, P. *Inorg. Chem.* **2006**, *45*, 2038.

(14) Tang, W.; Yang, X.; Liu, Z.; Ooi, K. *J. Mater. Chem.* **2003**, *13*, 2989.

(15) Ren, Y.; Armstrong, A. R.; Jiao, F.; Bruce, P. G. *J. Am. Chem. Soc.* **2010**, *132*, 996 PMID: 20039669.

(16) Tompsett, D. A.; Parker, S. C.; Bruce, P. G.; Islam, M. S. *Chem. Mater.* **2013**, *25*, 536.

(17) Devaraj, S.; Munichandraiah, N. *J. Phys. Chem. C* **2008**, *112*, 4406.

(18) Zang, J.; Li, X. *J. Mater. Chem.* **2011**, *21*, 10965.

(19) Liu, X.; Xu, H.; Lu, L.; Gong, L.; Yao, W.; Qu, B. *Mater. Lett.* **2012**, *79*, 39.

(20) Jiang, H.; Sun, T.; Li, C.; Ma, J. *J. Mater. Chem.* **2012**, *22*, 2751.

(21) Dubal, D. P.; Holze, R.; Kulal, P. M. *J. Mater. Sci.* **2013**, *48*, 714.

(22) Zhang, X.; Yu, P.; Zhang, H.; Zhang, D.; Sun, X.; Ma, Y. *Electrochim. Acta* **2013**, *89*, 523.

(23) (a) Bruce, P. G.; Freunberger, S. A.; Hardwick, L. J.; Tarascon, J.-M. *Nat. Mater.* **2012**, *11*, 19. (b) Thotiyl, M. M. O.; Freunberger, S. A.; Peng, Z.; Chen, Y.; Liu, Z.; Bruce, P. G. *Nat. Mater.* **2013**, *12*, 1049.

(24) Girishkumar, G.; McCloskey, B.; Luntz, A. C.; Swanson, S.; Wilcke, W. *J. Phys. Chem. Lett.* **2010**, *1*, 2193.

(25) Ogasawara, T.; Debart, A.; Holzapfel, M.; Novak, P.; Bruce, P. G. *J. Am. Chem. Soc.* **2006**, *128*, 1390.

(26) Debart, A.; Bao, J.; Armstrong, G.; Bruce, P. G. *J. Power Sources* **2007**, *174*, 1177. 13th International Meeting on Lithium Batteries, Biarritz, France, June 18−23, 2006.

(27) Lu, Y.-C.; Xu, Z.; Gasteiger, H. A.; Chen, S.; Hamad-Schifferli, K.; Shao-Horn, Y. *J. Am. Chem. Soc.* **2010**, *132*, 12170.

(28) McCloskey, B. D.; Scheffler, R.; Speidel, A.; Bethune, D. S.; Shelby, R. M.; Luntz, A. C. *J. Am. Chem. Soc.* **2011**, *133*, 18038.

(29) Thapa, A. K.; Hidaka, Y.; Hagiwara, H.; Ida, S.; Ishihara, T. *J. Electrochem. Soc.* **2011**, *158*, A1483.

(30) Freunberger, S. A.; Chen, Y.; Peng, Z.; Griffin, J. M.; Hardwick, L. J.; Bardé, F.; Novák, P.; Bruce, P. G. *J. Am. Chem. Soc.* **2011**, *133*, 8040.

(31) Xiao, J.; Hu, J.; Wang, D.; Hu, D.; Xu, W.; Graff, G. L.; Nie, Z.; Liu, J.; Zhang, J.-G. *J. Power Sources* **2011**, *196*, 5674.

(32) Xu, W.; Viswanathan, V. V.; Wang, D.; Towne, S. A.; Xiao, J.; Nie, Z.; Hu, D.; Zhang, J.-G. *J. Power Sources* **2011**, *196*, 3894.

(33) Mizuno, F.; Nakanishi, S.; Kotani, Y.; Yokoishi, S.; Iba, H. *Electrochemistry* **2010**, *78*, 403. 50th Battery Symposium in Japan, Kyoto, Japan, Nov 30−Dec 02, 2009.

(34) Jung, H.-G.; Hassoun, J.; Park, J.-B.; Sun, Y.-K.; Scrosati, B. *Nat. Chem.* **2012**, *4*, 579.

(35) Peng, Z.; Freunberger, S. A.; Chen, Y.; Bruce, P. G. *Science* **2012**, *337*, 563.

(36) Roche, I.; Chainet, E.; Chatenet, M.; Vondrak, J. *J. Phys. Chem. C* **2007**, *111*, 1434.

(37) Eary, L. E.; Rai, D. *Environ. Sci. Technol.* **1987**, *21*, 1187.

(38) Weaver, R. M.; Hochella, M. F.; Ilton, E. S. *Geochim. Cosmochim. Acta* **2002**, *66*, 4119.

(39) Nesbitt, H.; Canning, G.; Bancroft, G. *Geochim. Cosmochim. Acta* **1998**, *62*, 2097.

(40) Zhu, M.; Paul, K. W.; Kubicki, J. D.; Sparks, D. L. *Environ. Sci. Technol.* **2009**, *43*, 6655.

(41) El-Deab, M. S.; Awad, M. I.; Mohammad, A. M.; Ohsaka, T. *Electrochem. Commun.* **2007**, *9*, 2082.

(42) Gardner, S. D.; Hoflund, G. B.; Schryer, D. R.; Schryer, J.; Upchurch, B. T.; Kielin, E. J. *Langmuir* **1991**, *7*, 2135.

(43) Hoflund, G. B.; Gardner, S. D.; Schryer, D. R.; Upchurch, B. T.; Kielin, E. J. *Appl. Catal. B: Environ.* **1995**, *6*, 117.

(44) Busca, G.; Lietti, L.; Ramis, G.; Berti, F. *Appl. Catal. B: Environ.* **1998**, *18*, 1.

(45) Cheng, F.; Zhang, T.; Zhang, Y.; Du, J.; Han, X.; Chen, J. *Angew. Chem., Int. Ed.* **2013**, *52*, 2474.

(46) Oku, M.; Hirokawa, K.; Ikeda, S. *J. Electron Spectrosc. Relat. Phenom.* **1975**, *7*, 465.

(47) Tompsett, D. A.; Middlemiss, D. S.; Islam, M. S. *Phys. Rev. B* **2012**, *86*, 205126.

1425

dx.doi.org/10.1021/ja4092962 | *J. Am. Chem. Soc.* 2014, 136, 1418−1426

(48) Maphanga, R. R.; Parker, S. C.; Ngoepe, P. E. *Surf. Sci.* **2009**, *603*, 3184.

(49) Oxford, G. A. E.; Chaka, A. M. *J. Phys. Chem. C* **2011**, *115*, 16992.

(50) Oxford, G. A. E.; Chaka, A. M. *J. Phys. Chem. C* **2012**, *116*, 11589.

(51) Li, L.; Wei, Z.; Chen, S.; Qi, X.; Ding, W.; Xia, M.; Li, R.; Xiong, K.; Deng, Z.; Gao, Y. *Chem. Phys. Lett.* **2012**, *539*, 89.

(52) Trahey, L.; Karan, N. K.; Chan, M. K. Y.; Lu, J.; Ren, Y.; Greeley, J.; Balasubramanian, M.; Burrell, A. K.; Curtiss, L. A.; Thackeray, M. M. *Adv. Energy Mater.* **2013**, *3*, 75.

(53) Franchini, C.; Bayer, V.; Podloucky, R.; Parteder, G.; Surnev, S.; Netzer, F. P. *Phys. Rev. B* **2006**, *73*, 155402.

(54) Mellan, T. A.; Maenetja, K. P.; Ngoepe, P. E.; Woodley, S. M.; Catlow, C. R. A.; Grau-Crespo, R. *J. Mater. Chem. A* **2013**, *1*, 14879.

(55) Sayle, T. X.; Catlow, C. R. A.; Maphanga, R. R.; Ngoepe, P. E.; Sayle, D. C. *J. Cryst. Growth* **2006**, *294*, 118.

(56) Sayle, T. X. T.; Catlow, C. R. A.; Maphanga, R. R.; Ngoepe, P. E.; Sayle, D. C. *J. Am. Chem. Soc.* **2005**, *127*, 12828.

(57) Franchini, C.; Podloucky, R.; Paier, J.; Marsman, M.; Kresse, G. *Phys. Rev. B* **2007**, *75*, 195128.

(58) Cockayne, E.; Li, L. *Chem. Phys. Lett.* **2012**, *544*, 53.

(59) Catlow, C. R. A., Ed., *Computer Modelling in Inorganic Crystallography*; Academic Press: San Diego, CA, 1997.

(60) Hill, J. R. and Freeman, C. M. and Subramanian, L. In *Reviews in Computational Chemistry*; Liphowitz, K. B., Boyd, D. B., Eds.; Wiley: New York, 2000.

(61) Islam, M. A.; Fisher, C. A. J. *Chem. Soc. Rev.* **2014**, *43*, 185.

(62) Maphanga, R. R.; Sayle, D. C.; Sayle, T. X. T.; Ngoepe, P. E. *Phys. Chem. Chem. Phys.* **2011**, *13*, 1307.

(63) Sayle, T. X. T.; Maphanga, R. R.; Ngoepe, P. E.; Sayle, D. C. *J. Am. Chem. Soc.* **2009**, *131*, 6161.

(64) Watson, G. W.; Kelsey, E. T.; de Leeuw, N. H.; Harris, D. J.; Parker, S. C. *J. Chem. Soc., Faraday Trans.* **1996**, *92*, 433.

(65) Kresse, G.; Furthmüller, J. *Phys. Rev. B* **1996**, *54*, 11169.

(66) Perdew, J.; Burke, K.; Ernzerhof, M. *Phys. Rev. Lett.* **1996**, *77*, 3865.

(67) Nolan, M.; Parker, S. C.; Watson, G. W. *Surf. Sci.* **2005**, *595*, 223.

(68) Morgan, B. J.; Watson, G. W. *J. Phys. Chem. C* **2009**, *113*, 7322.

(69) Madsen, G. K. H.; Novak, P. *Europhys. Lett.* **2005**, *69*, 777.

(70) Schwarz, K.; Blaha, P. *Comput. Mater. Sci.* **2003**, *28*, 259.

(71) Ylvisaker, E. R.; Pickett, W. E.; Koepernik, K. *Phys. Rev. B* **2009**, *79*, 035103.

(72) Baur, W. *Acta Crystallagr. B* **1976**, *32*, 2200.

(73) Regulski, M.; Przeniosło, R.; Sosnowska, I.; Hoffmann, J.-U. *J. Phys. Soc. Jpn.* **2004**, *73*, 3444.

(74) Fritsch, S.; Navrotsky, A. *J. Am. Chem. Soc.* **1996**, *79*, 1761.

(75) Zheng, D.; Sun, S.; Fan, W.; Yu, H.; Fan, C.; Cao, G.; Yin, Z.; Song, X. *J. Phys. Chem. B* **2005**, *109*, 16439.

(76) Liang, S.; Teng, F.; Bulgan, G.; Zong, R.; Zhu, Y. *J. Phys. Chem. C* **2008**, *112*, 5307.

(77) Ji, Z.-H.; Dong, B.; Liu, Y.-Q.; Liu, C.-G. *Mater. Res. Bull.* **2012**, *47*, 3377.

(78) Kim, I. Y.; Ha, H.-W.; Kim, T. W.; Paik, Y.; Choy, J.-H.; Hwang, S.-J. *J. Phys. Chem. C* **2009**, *113*, 21274.

(79) Zhang, W.; Wang, H.; Yang, Z.; Wang, F. *Colloids Surf., A* **2007**, *304*, 60.

(80) Kalubarme, R. S.; Cho, M.-S.; Yun, K.-S.; Kim, T.-S.; Park, C.-J. *Nanotechnology* **2011**, *22*, 395402.

(81) Lu, X.; Zheng, D.; Zhai, T.; Liu, Z.; Huang, Y.; Xie, S.; Tong, Y. *Energy Environ. Sci.* **2011**, *4*, 2915.

(82) Wang, L.-C.; Liu, Y.-M.; Chen, M.; Cao, Y.; He; Fan, K.-N. *J. Phys. Chem. C* **2008**, *112*, 6981.

(83) Jia, Y.; Xu, J.; Zhou, L.; Liu, H.; Hu, Y. *Mater. Lett.* **2008**, *62*, 1336.

(84) Zhang, X.; Yang, W.; Yang, J.; Evans, D. G. *J. Cryst. Growth* **2008**, *310*, 716.

(85) Guan, H.; Chen, G.; Zhu, J.; Wang, Y. *J. Alloys Compd.* **2010**, *507*, 126.

(86) Qian, D.; Hinuma, Y.; Chen, H.; Du, L.-S.; Carroll, K. J.; Ceder, G.; Grey, C. P.; Meng, Y. S. *J. Am. Chem. Soc.* **2012**, *134*, 6096.

(87) Stampfl, C.; Ganduglia-Pirovano, M. V.; Reuter, K.; Scheffler, M. *Surf. Sci.* **2002**, *500*, 368.

(88) Hummelshoj, J. S.; Blomqvist, J.; Datta, S.; Vegge, T.; Rossmeisl, J.; Thygesen, K. S.; Luntz, A. C.; Jacobsen, K. W.; Norskov, J. K. *J. Chem. Phys.* **2010**, *132*, 071101.

(89) Xu, Y.; Shelton, W. A. *J. Chem. Phys.* **2010**, *133*, 024703.

(90) Xu, Y.; Shelton, W. A. *J. Electrochem. Soc.* **2011**, *158*, A1177.

(91) Ganduglia-Pirovano, M. V.; Hofmann, A.; Sauer, J. *Surf. Sci. Rep.* **2007**, *62*, 219.

(92) Poinsignon, C.; Djurado, E.; Klein, H.; Strobel, P.; Thomas, F. *Electrochim. Acta* **2006**, *51*, 3076.

(93) Sato, H.; Enoki, T.; Isobe, M.; Ueda, Y. *Phys. Rev. B* **2000**, *61*, 3563.

(94) Luo, F.; Song, W.; Yan, C.-H. *Chem. Phys. Lett.* **2006**, *431*, 337.

(95) Radin, M. D.; Rodriguez, J. F.; Tian, F.; Siegel, D. J. *J. Am. Chem. Soc.* **2012**, *134*, 1093.